Research article

Photocatalytic degradation of methylene blue by TiO$_2$/Nd$_2$O$_3$ composite thin films

Guodong Liu [a], Mamatrishat Mamat [a,*], Yiliyasi Baikeli [b,**], Xiaoshuo Dong [a]

[a] School of Physics and Technology, Xinjiang University, Urumqi, Xinjiang, 830017, PR China
[b] College of Chemistry and Chemical Engineering, Dezhou University, Dezhou, 253023, PR China

ABSTRACT

To improve the photocatalytic property of TiO$_2$ thin films, the composite thin films of TiO$_2$/Nd$_2$O$_3$ structure were fabricated by electron-beam physical vapor deposition method, and the photocatalytic property of the fabricated films was experimentally studied in the present work. The XRD and Raman analyses show that the TiO$_2$/Nd$_2$O$_3$ films are mainly hexagonal crystalline phase of Nd$_2$O$_3$. The XPS analysis for the chemical state changes of Ti, O and Nd of the basic elements in the films is confirming the electron flow in the internal electric field which generated in the TiO$_2$/Nd$_2$O$_3$ films. The surface morphology shows the lattice distortion which affects the changes in the energy band structure. Moreover, the formation of n-n homojunctions improved the separation efficiency of electrons and holes, and enhanced the catalytic activity. The photocatalytic performance for the methylene blue target dye shows that the sample with TiO$_2$ thickness of 20–25 nm has better performance, high degradation efficiency and high reaction rate.

1. Introduction

Titanium dioxide (TiO$_2$) is one of the widely studied and applied catalytic materials [1]. Since its photocatalytic performance is limited by the large forbidden bandwidth and high photogenerated electron-hole complexation rate, in order to improve the catalytic performance of TiO$_2$, researchers have proposed two methods, i.e., doping and constructing heterojunction. Among them, the constructing heterojunction is an effective method to enhance carrier separation by generating an internal electric field [2]. Since the energy levels of the two composite semiconductor films can effectively separate and reduce the photoelectron-hole binding rate, thus improving their photocatalytic performance[3]. Such bilayer composite semiconductor nanofilms have the advantages of controllable structure, uniform surface, good light absorption performance and obvious interfacial properties[4,5]The main semiconductor materials that commonly used to composite with TiO$_2$ are ZnO, SnO$_2$, TeO$_2$, GaAs, WO$_3$, V$_2$O$_5$, Fe$_2$O$_3$ and so on [6]. Researchers have extensively studied the above semiconductor materials to construct two-dimensional thin-film materials with different configurations by choosing different substrates (see Table 1 [7–16] for the preparation methods and thicknesses of various configurations). Compared with the commonly used semiconductor materials, relatively few studies have been conducted on Nd$_2$O$_3$.The report that Nd$_2$O$_3$ can be used as a catalytic material proves that Nd$_2$O$_3$ has a great potential for photocatalytic degradation [17]. In our work, to improve the photocatalytic degradation performance of TiO$_2$, the thin-film laminate structure of Si–Nd$_2$O$_3$–TiO$_2$ is designed. The thickness of Si is

---

725 μm, and the total thickness of Nd_2O_3–TiO_2 is determined to be 100 nm. By adjusting the thickness ratio between the two layers, can optimizing the optical and photocatalytic performance. In the present study, the pure TiO_2, Nd_2O_3, and composite TiO_2/Nd_2O_3 thin films were fabricated by electron-beam physical vapor deposition (EB-PVD) method, and their physicochemical properties were systematically investigated in detail at first. Then, the photocatalytic degradation efficiency of the heterojunction structures is further studied. Finally, the heterojunctions construction of TiO_2 and Nd_2O_3 is also ulteriorly studied accordingly for their applications [18] (see Table 1).

2. Experimental procedure

2.1. Preparation of thin films

In our experiment, TiO_2/Nd_2O_3 thin films were deposited on silicon (100) wafer substrates under vacuum conditions using EB-PVD method. The silicon wafers were ultrasonicated in anhydrous ethanol for 5 min, then ultrasonically washed with deionized water and acetone for 5 min, respectively, and finally rapidly air-dried with strong airflow. TiO_2 target (Gaoke Yurong New Material) with the particle size of 2 mm–6 mm and Nd_2O_3 target with the particle size of 3 mm–5 mm were selected for the deposition of TiO_2/Nd_2O_3 films. The size of silicon wafer is 19 cm*19 cm*725 μm. The parameters of filament current and beam current are respectively 0.58 A, and 0.32 A for the electron beam evaporating system. Prior to each deposition experiment, the deposition chamber was evacuated to a vacuum level below $1*10^{-6}$ Torr. The deposited thickness of every sample is 100 nm, i.e., the pure TiO_2(100 nm), and Nd_2O_3(100 nm), and also the compound structure of TiO_2 (5 nm)/Nd_2O_3 (95 nm), TiO_2 (10 nm)/Nd_2O_3 (90 nm), TiO_2 (15 nm)/Nd_2O_3 (85 nm), TiO_2 (20 nm)/Nd_2O_3 (80 nm), TiO_2 (25 nm)/Nd_2O_3 (75 nm) and TiO_2 (30 nm)/Nd_2O_3 (70 nm) samples (as shown in Fig. 1), totally eight types of samples. The eight samples except from TiO_2 and Nd_2O_3 were numbered by 1–6, which are 1-(TiO_2 (5 nm) -Nd_2O_3 (95 nm)), 2-(TiO_2 (10 nm) -Nd_2O_3 (90 nm)), 3-(TiO_2 (15 nm) -Nd_2O_3 (85 nm)), 4-(TiO_2 (20 nm) -Nd_2O_3 (80 nm)), 5-(TiO_2 (75 nm) -Nd_2O_3 (75 nm)), 6-(TiO_2 (30 nm) -Nd_2O_3 (70 nm)).the samples were annealed in a high-temperature tube furnace (OTF-1200) at 700 °C for 30 min in a nitrogen (N_2) atmosphere, while the N_2 airflow rate was kept at 120 cc. The thermal annealing temperature was set to rise 5 °C per minute.

2.2. Characterizations

After deposition, the necessary characterization was carried out to explore the physical properties of the Nd_2O_3/TiO_2 films. The thickness of all films, was in the range of 100 ± 20 nm. The crystal structure of the films was investigated using a Bruker D8 Advance X-ray diffractometer ($\lambda = 1.54$ Å), Germany. The x-ray data of all the samples were recorded at a scanning speed of 2°/min between 20° and 60°. The thin film lattice structure of the films was also investigated using Renishaw inVia Reflex Raman spectrometer, UK. The Laser was selected to be532 nm with a beam range of 100–3500 cm^{-1}. Changes in the chemical state of the films were investigated using Thermo Fisher Scientific ESCALAB250Xi X-ray photoelectron spectrometer, USA. The surface morphology of the films was investigated using a Hitachi su8010 field emission scanning electron microscope (FESEM). The surface roughness of the thin films was investigated using a Bruker Dimension ICON atomic force microscope. Transmission spectra were obtained at room temperature using a LAMBDA 650 PERKINELMER UV–Vis spectrophotometer in the wavelength range of 200–800 nm.

2.3. Photocatalytic activity measurement

The photocatalytic activity of Nd_2O_3/TiO_2 thin films was investigated by determining the degradation of methylene blue (MB) aqueous solution under UV irradiation. MB was chosen as a model dye in this study because it is a non-biodegradable organic pollutant. The TiO_2 catalyst was used for the degradation of MB solution, and initial solutions with concentrations of 5 mg/L, and 20 mg/L were prepared. To establish the adsorption-desorption equilibrium; the solutions were left in the dark for 30 min before UV irradiation. Photocatalytic experiments were carried out in glass test tubes at room temperature, and the mercury lamp light source was kept 10 cm above the periphery of the beaker. Nd_2O_3/TiO_2 films deposited on 19 mm × 19 mm (100) crystal oriented wafer substrates were

Table 1
Comparison of different configurations.

| Composite film configuration	Preparation method	Substrates	Film thickness (nm)
Ag/TiO_2 [16]	PVD	Textile	Ti (42)
Cu_2O/TiO_2/Pt [11]	PVD	Glass	80/120/18
TiO_2–SiO_2 [9]	PLD	F–SnO_2/glass	100
$P_2W_{16}Mo_2$/PVA/TiO_2 [14]	sol-gel	glass	–
PLA/TiO_2 [12]	sol-gel	PLA	–
TiO_2/Au/TiO_2 [8]	RF and DC	glass	20/2–4/20
TiO_2/Bi_2S_3 [10]	hydrothermal	FTO	2.5 μm
TiO_2/Fe_2O_3 [7]	sol-gel	stainless steel	–
TIO_2/SPI [13]	sol-gel	SPI	–
TiO_2/SLG [15]	CVD	Si	–
Nd_2O_3/TiO_2 (This work)	EB-PVD	Si(100)	100
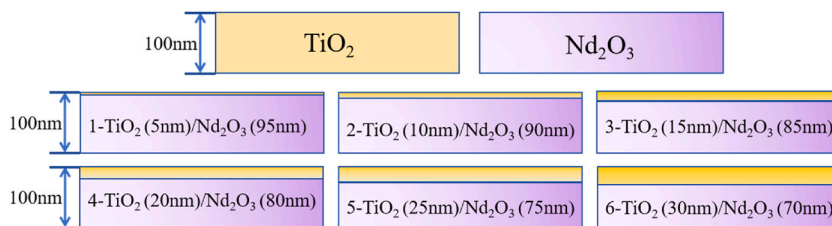
Fig. 1. The designed thickness and structure of all the samples.

immersed in the MB solution. The aqueous solution in the beaker was irradiated with a 500 w high-pressure mercury lamp. The irradiated solution was collected at intervals of 4 ml each time, and the concentration of MB in the solution was monitored by recording the intensity of the corresponding absorbance peaks as a function of reaction time with a UV–visible.

The degradation reaction was almost saturated near the 3 h. The degradation rate (η) of MB was calculated using equation (1):

$$\eta = C_0 - C/C_0 \times 100\% = A_0 - A/A_0 \times 100\%. \tag{1}$$

Where the C_0 and A_0 are the initial concentration and absorbance of MB solution at 664 nm, respectively. C and A are the concentration and absorbance of MB solution at 664 nm under UV irradiation, respectively. The blank and dark experiments were corrected as the perturbations generated by the UV radiation and film adsorption, respectively.

3. Results and discussion

3.1. XRD pattern analysis and Raman profiling

Fig. 2 show the XRD patterns of TiO_2 and Nd_2O_3 thin film samples with thermal annealed at the temperature of 700 °C. In Fig. 2, the main characteristic peak of TiO_2 thin film sample is at the 2θ of 25.5° which is corresponding to the (101) crystal plane of TiO_2 anatase phase. While, the main characteristic peak of the Nd_2O_3 thin film is at the 2θ of 26.8° [19], which corresponds to the (110) crystal plane of the hexagonal phase of the Nd_2O_3 film [20](Nd_2O_3 JCPDS card No. 01-074-1147、TiO_2 JCPDS card No. 01-075-2552、Si JCPDS card No. 01-080-0018).

The crystal structures of TiO_2/Nd_2O_3 thin films with different composite thicknesses were characterized by XRD, as shown in Fig. 3. According to the distribution of diffraction peaks, the diffraction peaks are located at 26.86°and 30.76°, corresponding to the (100) and (011) faces of the hexahedral structure. The diffraction peaks in the figure appear at 46.21°,47.69°,54.62°,55.46° and 56.38°, corresponding to (220), (−314), (−352) and (311) surfaces of crystalline silicon (Si), respectively.

Analyzing the diffraction peaks of (1)–(6) for six samples, it is found that the peak positions and diffraction intensities for the different samples remain unchanged except for the diffraction peaks at the 2θ of 26.86° and 30.76°, where the peak positions and diffraction intensities change with the different samples. These two diffraction peaks are shifted and broadened with the thickness of TiO_2 layer. From sample (1) to sample (3), the diffraction peak at the 2θ of 26.86° shows a significant left shift and the diffraction peak at the 2θ of 30.76° shows a right shift. Some sharpening of the peak shape also occurs. From sample (3) to sample (6), the peak height gradually decreased and the peak shape gradually broadened. Although the sample is a composite sample of TiO_2 and Nd_2O_3, the diffraction peaks in the spectrum are mainly corresponding to Nd_2O_3, because of the Nd_2O_3 accounts for the main part of the sample.
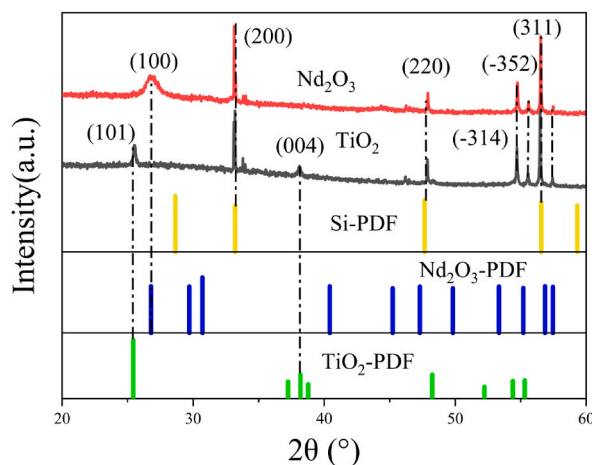

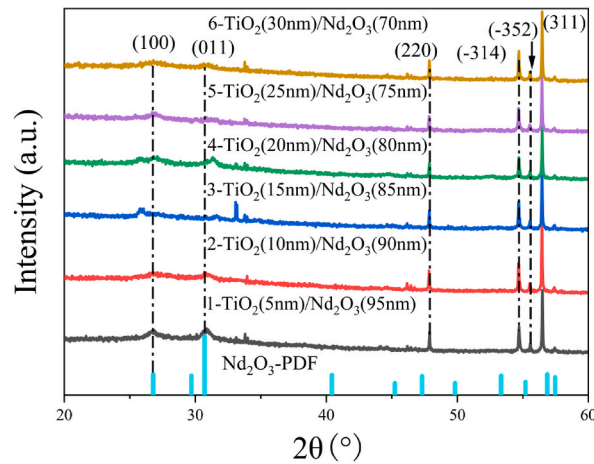**Fig. 2.** XRD patterns of TiO_2 and Nd_2O_3 thin film samples.

Fig. 3. XRD profiles of (a) TiO$_2$(5 nm)/Nd$_2$O$_3$(95 nm), (b) TiO$_2$(10 nm)/Nd$_2$O$_3$(90 nm), (c) TiO$_2$(15 nm)/Nd$_2$O$_3$(85 nm), (d) TiO$_2$(20 nm)/Nd$_2$O$_3$(80 nm), (e) TiO$_2$(25 nm)/Nd$_2$O$_3$(75 nm), (f) TiO$_2$(30 nm)/Nd$_2$O$_3$(70 nm) samples.

In the XRD analysis, the left-right shift of the peak position is related to the change of the crystal plane of the sample, and the distance of the crystal plane becomes larger by moving to the left, while the peak shifted to the left is usually pointing to a small angle shift, which means that the lattice constant becomes larger, and the usual reason is likely to be: when the two kinds of materials are annealed at the high temperature of 700 °C, van der Waals bonding occurs at the junction of the two kinds of materials, while both are undefined phases prepared by EB-PVD without thermal annealing. The result also provides conditions for the composite of the two kinds of layers.

As the lattice constants of TiO$_2$ and Nd$_2$O$_3$ are different, the lattice constant of Nd layer is also larger than that of Ti layer, so the two kinds of layers are combined to produce a lattice distortion. The result can be shown by the peak position changes in Fig. 3. The lattice distortion also proves the existence of macroscopic residual stresses between the two layers. Macroscopic residual stresses may cause anisotropic contraction of the lattice, displacing the peaks at a large angle for the compressive stresses and at a small angle for the tensile stresses. Additionally, the result also corresponds to the broadening of the peak shape that indicates the crystal phase is not very good and the consistency of the crystal is very poor. In this case, the samples of (3), (4), and (5) correspond to a better crystal pattern. However, a significant peak shift occurs for the sample (3) compared to the other two samples of (4) and (5). When the thickness of TiO$_2$ layer reaches 30 nm (sample (6)), all the peak positions turn to the normal. The result indicates that TiO$_2$ begins to affect the crystal structure of Nd$_2$O$_3$ only when the thickness of TiO$_2$ exceeds 15 nm. When the thickness reaches 30 nm, i.e., for the sample of (6), a stable crystalline phase is produced and TiO$_2$ no longer affects the crystal of Nd$_2$O$_3$.
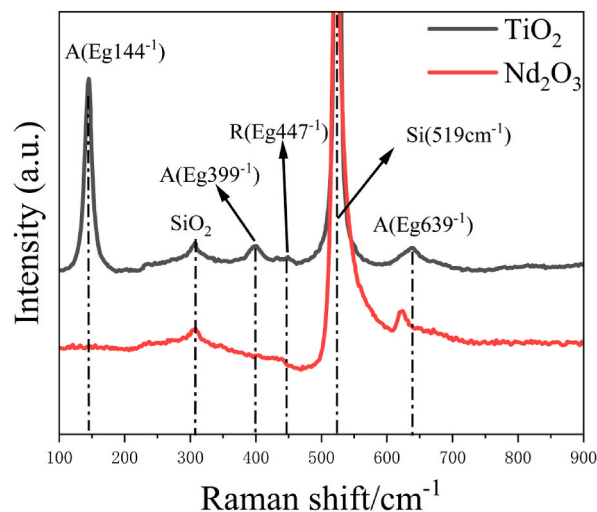

Fig. 4. Raman plots of TiO$_2$ and Nd$_2$O$_3$ thin film samples.

3.2. Raman profiling

The telescopic vibration peaks of TiO_2 and Nd_2O_3 thin film samples are shown in Fig. 4. According to the literature [21,22], the anatase phase of TiO_2 contains six Raman vibrational modes of A1g+2B1g+3g, and the corresponding Raman vibrational peaks are at the wavelength of 519 cm^{-1} (A1g+2B1g, $\nu1+\nu2$), 399 cm^{-1} (B1g, $\nu3$), 639 cm^{-1} (Eg, $\nu4$), 199 cm^{-1} (Eg, $\nu5$), and 144 cm^{-1} (Eg, $\nu6$), respectively. While, the rutile phase of TiO_2 correspond to four Raman vibrational modes: A1g + B1g + B2g, the vibrational peaks are at the wavelengths of 612 cm^{-1} (A1g, $\nu1$), 143 cm^{-1} (B1g, $\nu2$), 826 cm^{-1} (B2g, $\nu3$) and 447 cm^{-1} (Eg, $\nu4$) respectively. In Fig. 3, the TiO_2 thin film samples deposited by EB-PVD mainly exhibit four Raman peaks at the wavelength of 144 cm^{-1}, 399 cm^{-1}, 447 cm^{-1} and 639 cm^{-1}. The result is consistent with the XRD result of the diffraction peaks for the anatase phase. In contrast, the Nd_2O_3 thin film sample has no obvious Raman peaks. Meanwhile, both samples have Raman peaks at the 300 cm^{-1}, which is since the oxygen element of Nd_2O_3 reacts with the silicon element of the substrate to form valence bonds, so the corresponding diffraction peaks of SiO_2 appear in the spectra.

The crystal structures of TiO_2/Nd_2O_3 films with different composite thicknesses were characterized by Raman spectra as shown in Fig. 5. As can be seen from Fig. 4, Nd_2O_3 exhibits no relevant characteristic peaks in the map, while the TiO_2 film exhibits obvious characteristic peaks of anatase and rutile phases. Therefore, all the characteristic peaks in the spectra of Fig. 5 are about the characteristic peaks of TiO_2. Because the Raman spectrum directly reflects the vibrational modes of the sample structure (Eg + B1g + A1g), where Eg represents the symmetric telescopic vibration and directly reflects the change of the oxygen sublattice in the TiO_2 structure, therefore can be aligned with the change of oxygen vacancy (O_v) defects in the crystals. The O_v will be analyzed in detail in the XPS analysis. B1g, on the other hand, represents the symmetric bending vibration, which reflects the change of Ti. In Fig. 5, Raman peaks can be seen at the wavelengths of 144 cm^{-1}, 301 cm^{-1} and 447 cm^{-1}. Since a silicon wafer was used as the substrate for the experiment, the peak at the 301 cm^{-1} in the spectra can be approved to the characteristic peak of silica, and the reason for its appearance is explained in the above section and will not be explained here.

From the Raman spectra mentioned above, the peaks at the 144 cm^{-1} and 447 cm^{-1} in the spectra represent the anatase phase, and the rutile phase, respectively. Since the peak at the 447 cm^{-1} does not change much compared to the peak at the 144 cm^{-1}, the main analysis is concentrated on the peak at the Eg 144 cm^{-1} [23]. When the TiO_2 thickness is 15 nm (sample 3) a characteristic peak at the 144 cm^{-1} occurs. When the TiO_2 thickness is 20 nm (sample 4) the characteristic peak at the 144 m^{-1} disappears. When the thickness continues to increase (sample 5) the characteristic peak of 144 cm^{-1} with the highest diffraction intensity appears in all the samples. When the thickness reaches 30 nm (sample 6), the characteristic peak is weaker than that of the previous sample. The result corresponds to the change in the XRD peaks of the individual samples in Fig. 3, and the Raman pattern also demonstrates that when the thickness of the surface TiO_2 layer reaches 30 nm, there is no further structural influence by the lower layer of Nd_2O_3 film [24].

3.3. XPS pattern analysis

Fig. 6 shows the XPS patterns of TiO_2 and Nd_2O_3 thin film samples. The spectra show the chemical states of all the elements of TiO_2 and Nd_2O_3 thin films. For TiO_2, additionally the C element used for the calibration of mainly Ti 2p and O 1s two elements of the chemical state. Among them, Ti 2p belongs to the spin-orbit splitting peaks (SOS), i.e., mainly the two peaks of Ti 2p$_{1/2}$ and Ti 2p$_{3/2}$ [25]. By fitting, it can be concluded that there are defects in the TiO_2 samples prepared by EB-PVD that contain Ti^{3+} ions. The defect is also reflected in the O 1s pattern of TiO_2 samples [26]. From the O 1s pattern, the three kinds of main chemical states of the O element, O^{2-}, O_v, and –OH/H_2O, are analyzed. The Nd_2O_3 thin film samples are characterized by the chemical states of the O 1s and Nd 3d chemical elements. The Nd3d is similar to Ti 2p, also belongs to the SOS, mainly two peaks of Nd 3d$_{3/2}$ and Nd 3d$_{5/2}$ [27]. However,
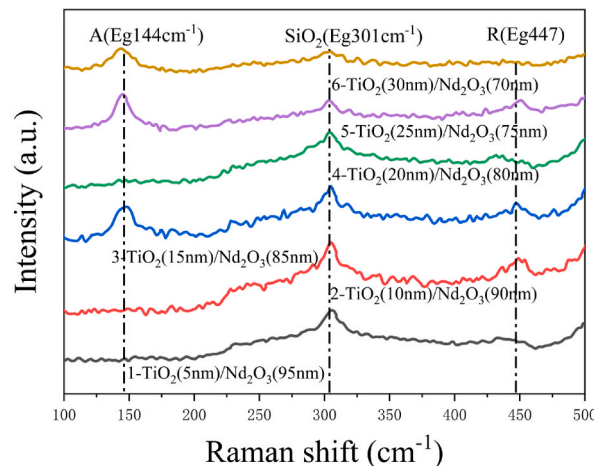

Fig. 5. Raman analysis profile of (a) TiO_2(5 nm)/Nd_2O_3(95 nm), (b) TiO_2(10 nm)/Nd_2O_3(90 nm), (c) TiO_2(15 nm)/Nd_2O_3(85 nm), (d) TiO_2(20 nm)/Nd_2O_3(80 nm), (e) TiO_2(25 nm)/Nd_2O_3(75 nm), (f) TiO_2(30 nm)/Nd_2O_3(70 nm).
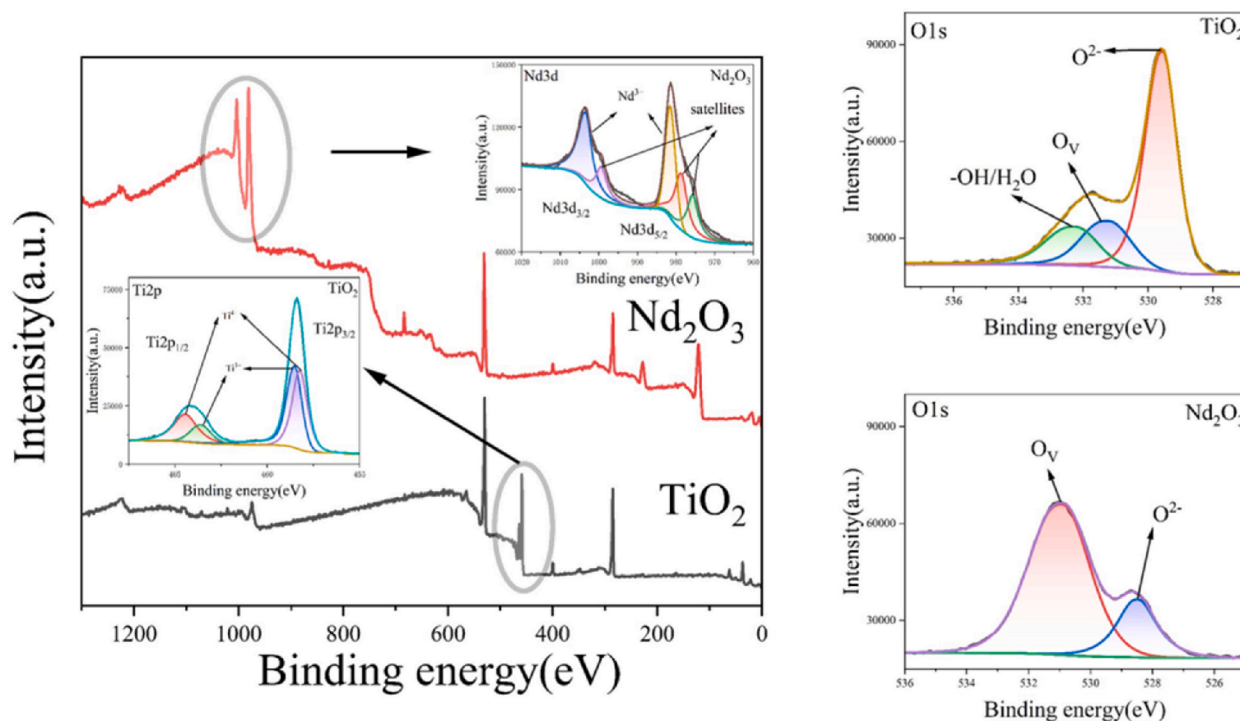
Fig. 6. XPS profiles of the TiO_2 and Nd_2O_3 thin-film samples.

because the conventional X-ray source is not monochromatic, but there are also some small companion lines with slightly higher energies, which leads to the figure profile. In addition to the main spectrum excited by $K_\alpha 1$, 2, there are some small companion peaks. Therefore, some of the companion peaks (satellite peaks) appear around the two Nd $3d_{3/2}$ and Nd $3d_{5/2}$ peaks in the Nd3d profile. Meanwhile, the O 1s of Nd_2O_3 mainly consist of two kinds of chemical states, O^{2-} and O_v, and the O_v of Nd_2O_3 occupies the major part of the chemical state of the oxygen compared with that of TiO_2. The result also proves the existence of a large number of defects in the Nd_2O_3 films thermal annealed at the temperature of 700 °C, which also provides a feasible condition for the change of the chemical
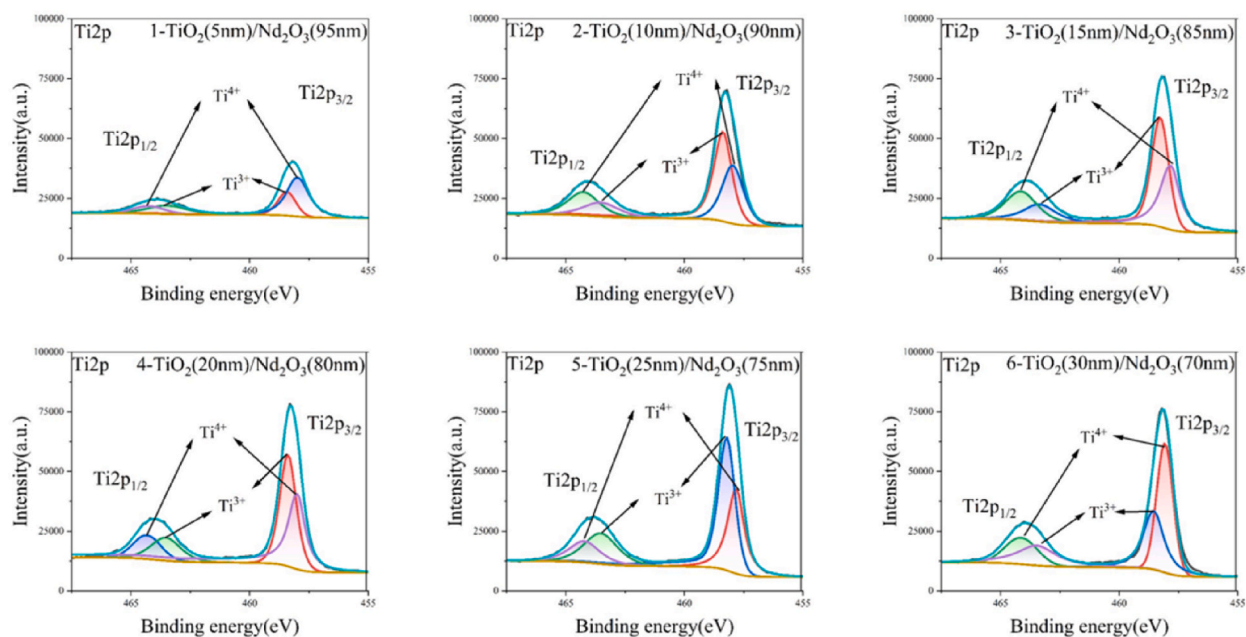

Fig. 7. X-ray photoelectron spectra, the Ti chemical states for the all samples.

state by the interfacial composite of the two kinds of materials.

Fig. 7 shows the plots of Ti 2p for the samples with the different thicknesses of TiO_2 and Nd_2O_3 composite layers. The thickness of TiO_2 film is increasing while the total thickness of the sample is constant. As the thickness of the TiO_2 film changes, the chemical state of the Ti element of the sample also changes. The diffraction intensity of the Ti $2p_{1/2}$ and Ti $2p_{3/2}$ peaks of Ti increases with increasing of the TiO_2 thickness. The diffraction intensity reaches its highest point when the thickness of the TiO_2 film is 25 nm, and then decreases when the thickness continues to increase. The variation trend of Ti^{3+} ion defects is reflected in the change of its own diffraction peaks. The result is consistent with the fact that when the TiO_2 film thickness is 30 nm, the lower layer of Nd_2O_3 will no longer influence on the upper layer of TiO_2 film, therefore gives the above-mentioned results of the chemical state variations of the samples.

Fig. 8 shows the O 1s profiles of the samples with various thicknesses of TiO_2 and Nd_2O_3 composite layers. The diffraction intensity of the O peaks increases with the increase of the TiO_2 layer thickness and reaches its highest point at 25 nm, and then decreases when the thickness of the TiO_2 layer continues to increase. The variation trend of O^{2-} reflected in the change of its own diffraction peak. O_v, on the other hand, reaches its maximum at a thickness of 20 nm. In contrast, the trend of $-OH/H_2O$ is opposite to that of O_v defects. The values of chemical state variation trends for the all the samples are quantified in Table 2.

Fig. 9 shows the Nd 3d maps of the samples with various thicknesses of TiO_2 and Nd_2O_3. The diffraction intensities of the Nd $3d_{3/2}$ and Nd $3d_{5/2}$ peaks of Nd increase with the decrease of the Nd_2O_3 layer thickness. The diffraction intensity reaches its highest point when the thickness is 85 nm, and the diffraction peaks gradually decrease when the thickness of Nd_2O_3 layer continues to decrease [28].

Comparison of the three types of Ti 2p, O 1s and Nd 3d maps of the six samples shows that the chemical state variations of the different thicknesses of TiO_2 layers agree with the chemical state variations of the corresponding thicknesses of Nd_2O_3 layers. From this, it can be learned that the chemical elements therein have a certain chemical shift. The reasons for the chemical shift are generally the following: 1. Different oxidation states occurred by forming the compound layers; 2. The emergence of a new kinds of compounds; 3. The production of a different lattice structure; 4. Different number of the close neighbors or atoms occupying a different position of the dot matrix. With the above reasons, the composition of the two kinds of materials not only causes the lattice distortion, but also produces the rows of compounds (Nd-*O*-Ti). The main factors affecting the chemical shift are electro-negativity and various anisotropy effects. In our work, the electro-negativity plays a major role, since the electro-negativity of Nd is 1.14 eV, which is not only smaller than the electro-negativity value of 1.54 eV for the Ti, but also smaller than the electro-negativity value of 3.44 eV for O. Therefore, the valence electrons of Nd are attracted to the nuclei of Ti and O in the composite structure. Moreover, when the density of the electron cloud around the nucleus of Nd is reduced, the shielding effect is also reduced, and the electron binding energy is increased, and at the same time, because of the loss of valence electrons, the activity of Nd ions is increased. In contrast, the Ti atom has a stronger ability to absorb electrons than Nd atom due to its greater electro-negativity than Nd atom, which has a smaller electro-negativity. Therefore, increases the electron cloud density outside the of nucleus, which improves the shielding effect and reduces the electron beam fugacity of Ti atoms. Thus, leads to the gradual increase of Ti^{3+} ion defects in the samples. Moreover, because of the thickness of 30 nm is the limit of the effect of the composition of the two kinds of materials, so Ti^{3+} ion defects instead decrease up to the thickness of 30 nm. To electric charge balancing accompanied by the changes in the chemical state of Ti ions, O_v in the chemical state of the element O also
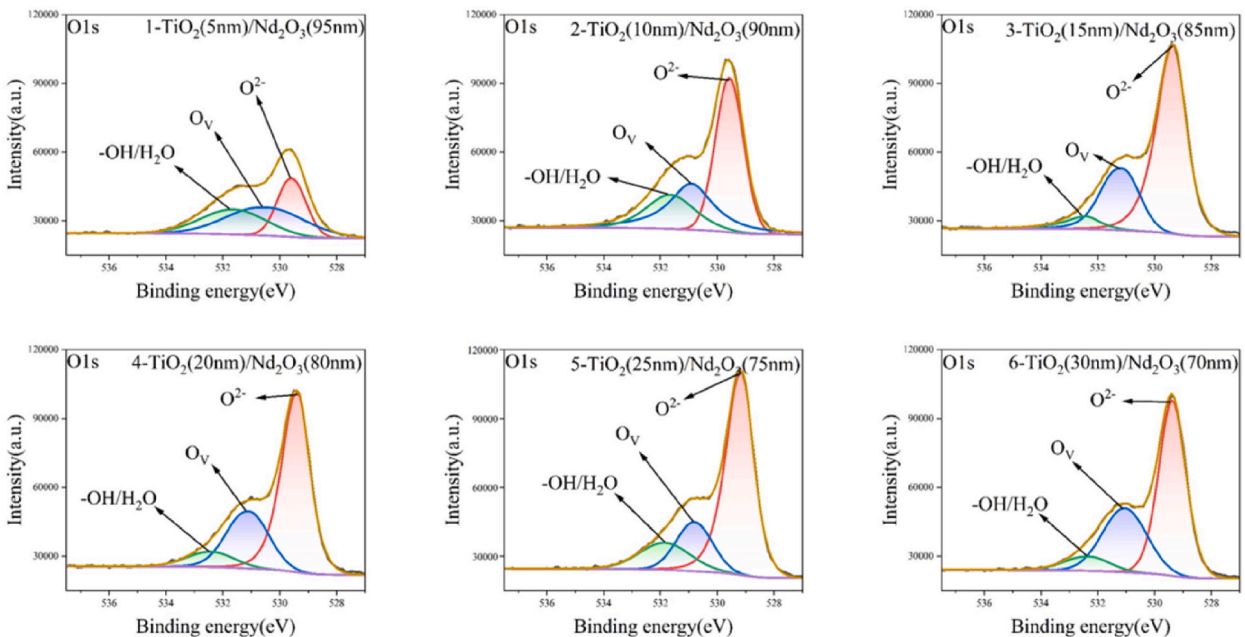

Fig. 8. X-ray photoelectron spectra, the O chemical states for the all samples.

Table 2
Area ratio of Ti and O chemical states in XPS patterns.

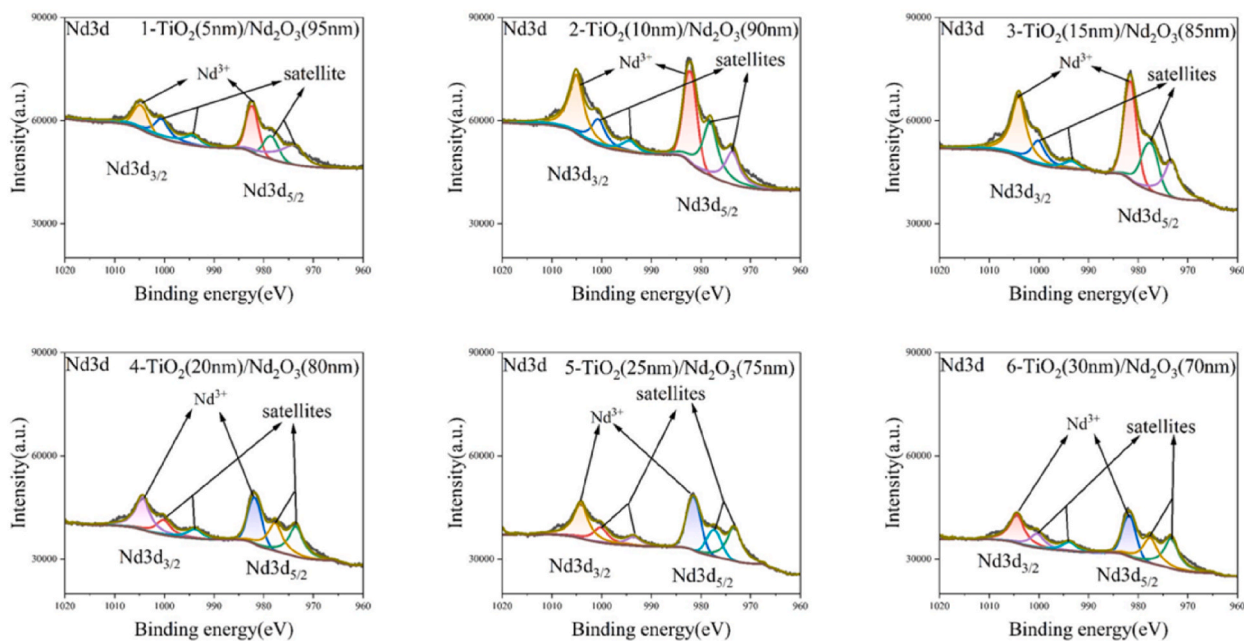| Samples	O^{2-} (Conc.%)	O_v (Conc.%)	-OH/H_2O (Conc.%)	Ti^{4+} (Conc.%)	Ti^{3+} (Conc.%)
1-TiO_2(5 nm)/Nd_2O_3(95 nm)	52.4	25.1	22.5	41.1	58.9
2-TiO_2(10 nm)/Nd_2O_3(90 nm)	65.8	19.7	14.5	44.0	56.0
3-TiO_2(15 nm)/Nd_2O_3(85 nm)	71.4	23.6	0.05	42.3	57.7
4-TiO_2(20 nm)/Nd_2O_3(80 nm)	71.0	22.7	6.3	42.4	57.6
5-TiO_2(25 nm)/Nd_2O_3(85 nm)	65.4	19.6	15.0	39.1	60.9
6-TiO_2(30 nm)/Nd_2O_3(70 nm)	73.0	17.5	9.5	37.3	62.7

Fig. 9. X-ray photoelectron spectra, the Nd chemical states for the all samples.

changes following with the changes in the Ti^{3+} ion defects. Meanwhile, the Nd_2O_3 film itself has a large number of O_v defects [29]. The lattice distortion produced by the composition of the two kinds of materials will cause different atoms to occupy the different clustered dot positions resulting in the different lattice structures, which will lead to the variation trend of O_v defects will not be completely accompanied by the variation trend of Ti^{3+} ion defects in the similar way.

3.4. SEM, AFM analysis

Figs. 10 and 11 are the SEM and AFM patterns of all the test samples, which show the surface morphology and roughness of all the samples at the resolution of 500 nm and 600 nm, respectively. As can be seen from Fig. 9, the TiO_2 films prepared by EB-PVD are a kind of flaky uniformly distributed and denser morphology, while the morphology of the Nd_2O_3 films is granular and uniformly distributed, meanwhile there are some crescent-shaped pores. The surface morphology of the composites changed following from the No. 1 to No. 6. The composite samples showed the agglomerated spots on the film surface compared to the previous a single layer material [30]. The distribution and the size of the clustered dots on the surface morphology varies with the thicknesses of the different composite layers. The variation in clustered dots and morphology are directly reflected in Fig. 11 of the AFM plot and Figss. 12–14. From the R_a (arithmetic average roughness), R_q (root-mean-square roughness) and R_{max} (distance between the highest and lowest points of the contour within the length), it can be seen that: the roughness of TiO_2 surface layer is higher than that of Nd_2O_3 surface, and the roughness of composite samples continues to increase with the increase of TiO_2 thickness [31]. The roughness of TiO_2 layer with the thickness of 15 nm reaches a maximum, and then continue to decrease with the thickness of TiO_2. With further increasing the thickness of TiO_2 layer as 30 nm, the roughness increase again [27]. Defects are a major factor affecting the photocatalytic performance of TiO_2 crystals, and the poor development of TiO_2 crystals and the defects in crystal lattice will reduce the photocatalytic performance of TiO_2 crystals, which is because defects are traps and recombination centers trapped in the deep layers of photogenerated electrons-holes. It can be seen from Figs. 12–14 that with the increase of the thickness of TiO_2, the roughness of samples of 1, 2 and 3 changes drastically, which is due to the lattice diffusion of the two materials after high temperature annealing, which causes lattice distortion, which leads to a large roughness on the surface of the test sample. This affects the photocatalytic activity of the sample and leads to the appearance
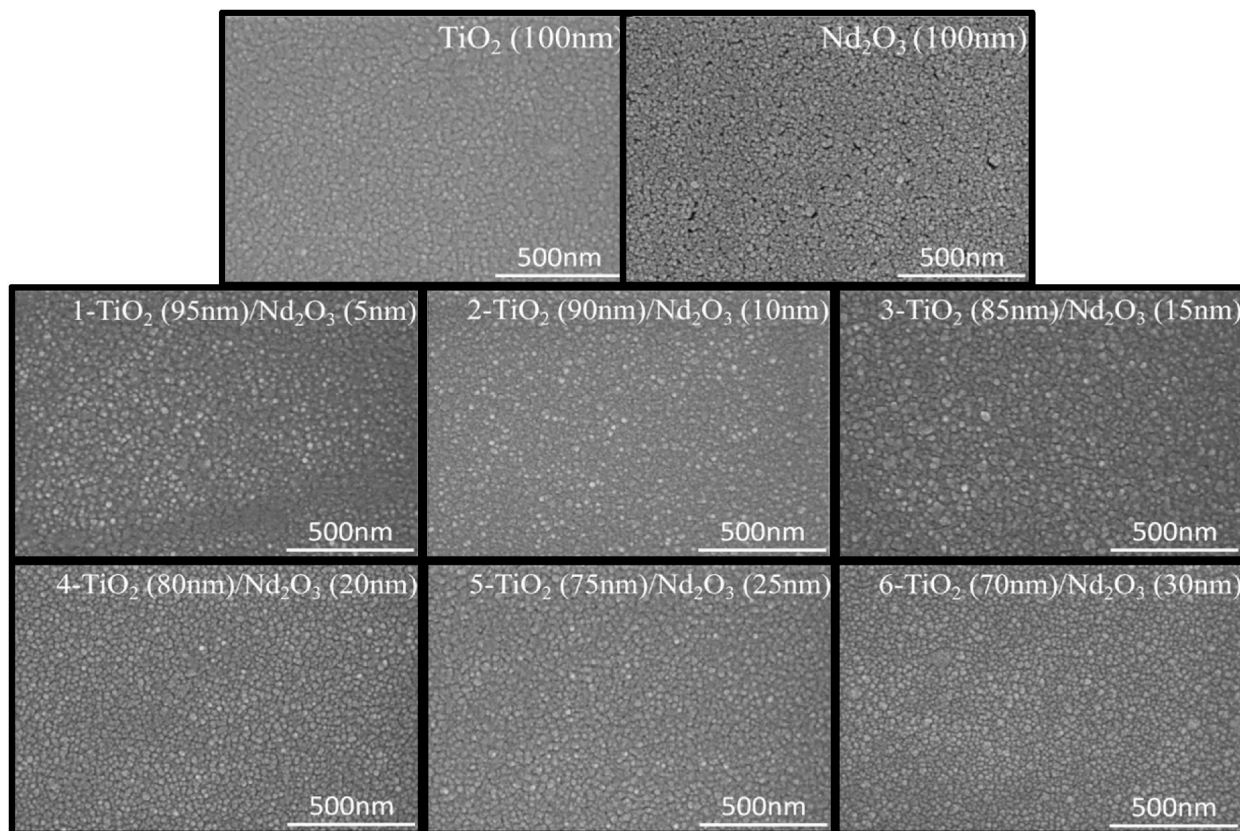
Fig. 10. SEM patterns of surface morphology for all the samples.

of oxygen vacancy defects in the sample. The introduction of oxygen vacancy defects is discussed in detail in the XPS analysis section, and will not be repeated in this section.

3.5. Optical analysis

The values of valence bands estimated as a work function for all the samples are shown in Fig. 15. The values of valence bands of TiO$_2$ and Nd$_2$O$_3$ are 2.42 eV, and 1.81 eV, respectively. The valence band values for the samples from No. 1–5 increase with the increase of the thickness of TiO$_2$ layer. The highest value of 2.89 eV for the valence band is found at the TiO$_2$ thickness of 25 nm and then decreases to 2.50 eV at the TiO$_2$ thickness of 30 nm, which is attributed to the presence of macroscopic residual stresses at the interfaces of the two kinds of materials, resulting in the lattice distortions. It is also related to the electron affinity and ionization energy of the different elements in the chemical composition of the materials [32]. These factors have a direct influence on the changes in the energy band structure. Fig. 16 illustrates the transmittance and forbidden bandwidth for all the samples. Relative to the absorption band edge of TiO$_2$ sample, all the composite samples undergo slightly blue shift [33,34]. The result is directly related to the forbidden bandwidth of the samples. The forbidden band widths of all the composite samples are mainly centered between the values of the forbidden bands of the pure TiO$_2$ and Nd$_2$O$_3$ samples [35]. When the thickness of the TiO$_2$ layer of the composite film is higher than 15 nm, the forbidden band widths of the samples do not change significantly. The change of the energy band size is mainly related to the change of the particle size, due to the quantum size effect, the energy gap becomes larger (the forbidden bandwidth increases) which caused by the smaller particle size [36,37]. Although, the nanoparticles also cause lattice distortion in the lattice, the Nd$_2$O$_3$ as being the main component, so the effect of TiO$_2$ on the lattice constant of the entire composite film become smaller. The distance between the first and second nearest neighbors becomes shorter, and the shortening of the valence bond length causes the bond intrinsic vibration frequency of the nanoparticles to increase. It would be mentioned that the light absorption bands are shifted to higher wavelengths region relative to the light absorption bands of Nd$_2$O$_3$.

3.6. Photocatalytic performance

Fig. 17a and c exhibit the time curves of the residual rate of MB solution at concentrations of 5 mg/L, 20 mg/L for the Nd$_2$O$_3$/TiO$_2$ composite samples with different conformal thicknesses, respectively. The degradation experiments were carried out under the irradiation of 500 W mercury lamp. The highest degradation rate of the sample 5-TiO$_2$ (25 nm)/Nd$_2$O$_3$ (75 nm) was achieved at the
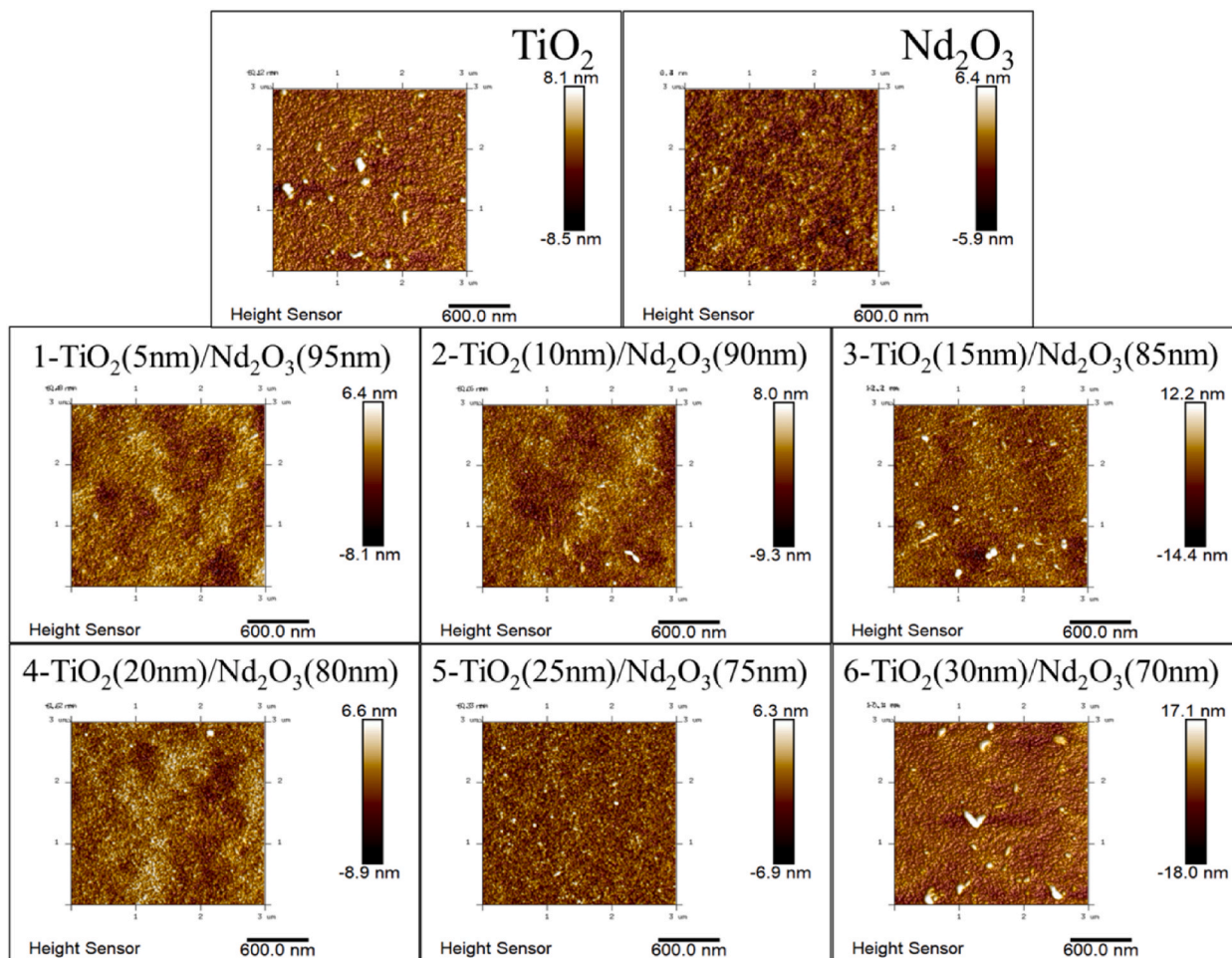
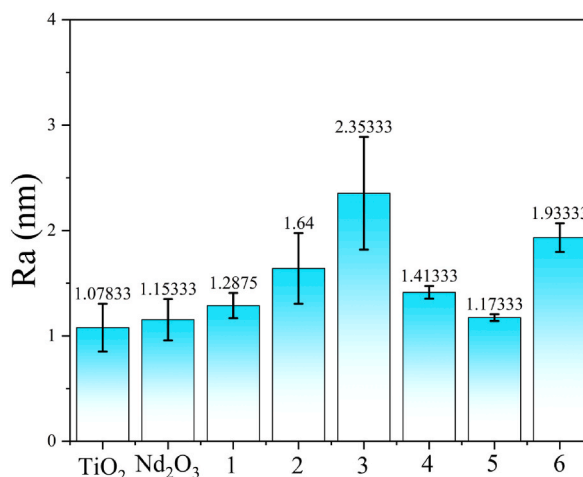**Fig. 11.** AFM profiles of surface morphology for all the samples.

Fig. 12. *Ra* values for all of the samples.

concentration of 5 ml/L of MB solution, and the degradation rate reached 91.8 %. Compared with the degradation rate of pure TiO_2 samples in MB solution at the same concentration value, the degradation rate increased by 14 %. The 5-TiO_2 (25 nm)/Nd_2O_3 (75 nm) sample also showed the highest degradation rate at 20 ml/L MB solution, with a degradation rate of nearly 72.9 %. Compared with the

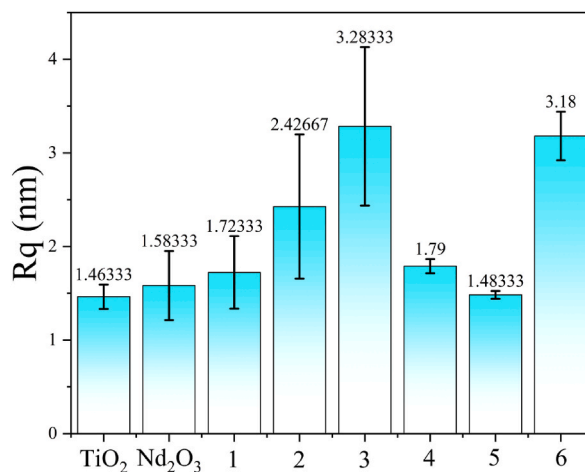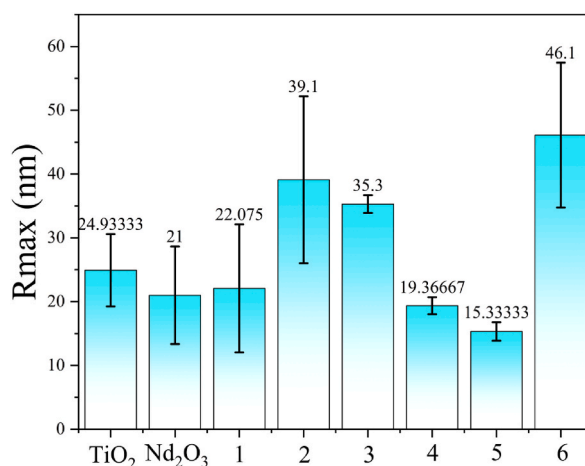**Fig. 13.** R_q values for all of the samples.

Fig. 14. R_{max} values for all of the samples.

degradation rate of pure TiO_2 at the same concentration value of MB solution, the degradation rate increased by 10.2 %. From the degradation results, it is clear that the catalytic performance of Nd_2O_3/TiO_2 heterojunction photocatalysts is significantly improved. The photocatalytic efficiency of the sample 5-TiO_2 (25 nm)/Nd_2O_3 (75 nm) photocatalyst was the highest among all Nd_2O_3/TiO_2 heterojunction photocatalysts. The experimental data in Figs. 17b and d clearly demonstrate the consistency of the results with the pseudo-first-order kinetic model [38].

3.7. Mechanism of improved photocatalytic activity

The energy band information of all the samples is demonstrated in the plots of Fig. 18. The figure shows that the valence band value of TiO_2 is higher than the valence band value of Nd_2O_3. While the conduction band value of TiO_2 is higher than the conduction band value of Nd_2O_3 [29]. Since the both of the materials are wide band gap n-semiconductors, so the heterojunction structure of the composite of the two materials can be called *n-n* homojunction [4]. Where Nd_2O_3 is n + -type semiconductor at the one side, and TiO_2 is *n-type semiconductor at the other side*. Since the n $^+$ -type side has more free electrons than *n*-type side, the internal concentration difference causes the electrons to flow from n^+ -type side to the *n*-type side [39]. As the electrons diffuse from the high concentration region to the low concentration region, the high concentration region is left with a positive charge (donor ion) that is not occupied by electrons, while the low concentration region develops a negative charge because of the extra electrons [40]. This charge distribution creates a built-in electric field near the contact region, which is directed from the n^+-type region to the n type region. The corresponding energy band change is clearly depicted in Fig. 19.

When irradiated with the light of the sufficient excitation energy, the inter-band transitions occur on the both sides. Meanwhile, due to the difference in the energy levels of the valence and conduction bands, the photogenerated electrons will be mainly concentrated in the conduction band of TiO_2, while the holes are concentrated in the valence band of Nd_2O_3. The result leads to the
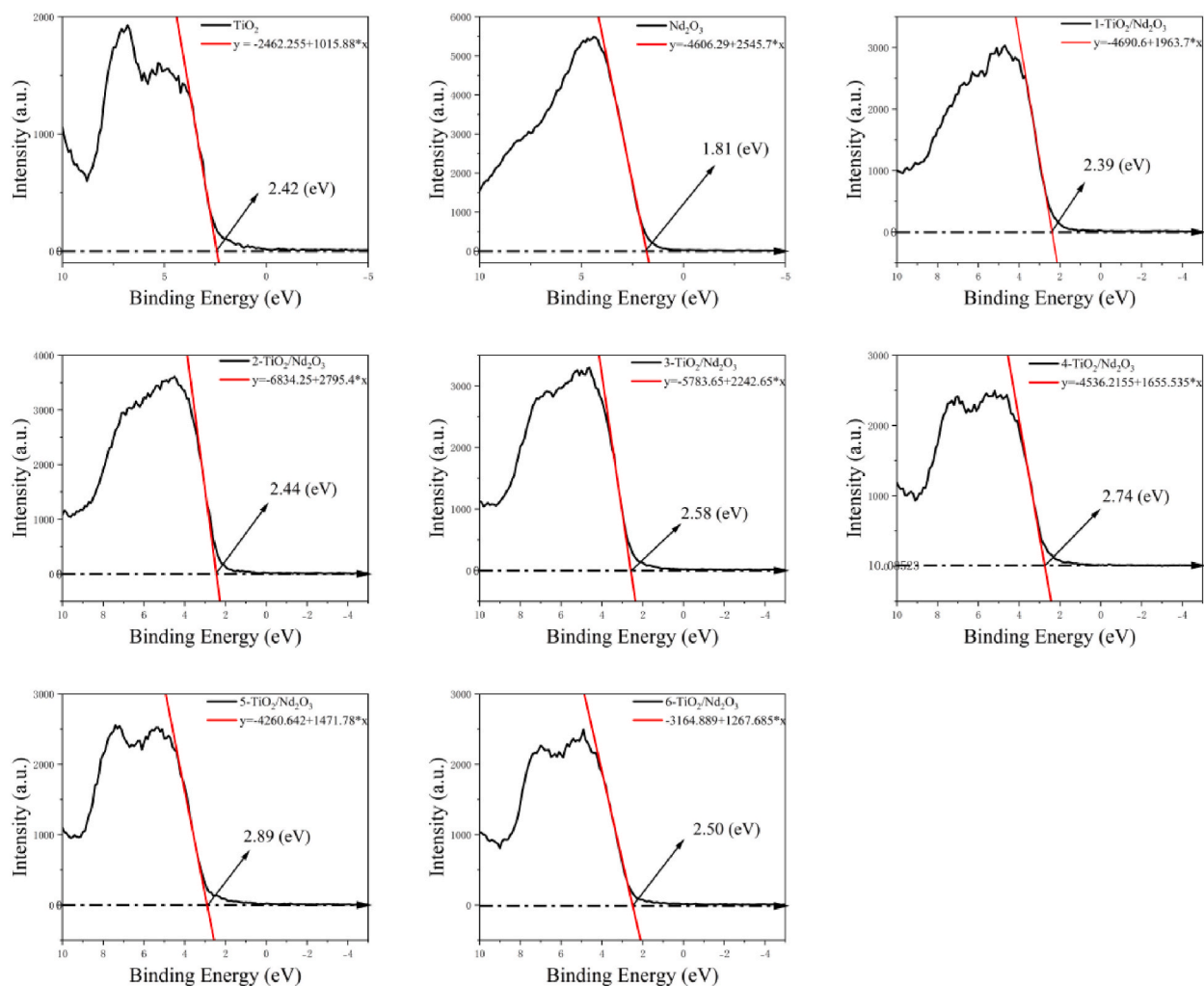
Fig. 15. Valence band value estimation from binding energy.

photogenerated carriers are separated and given longer lifetimes, which can improve the quantum efficiency and reduces the photon-hole complexation rate, and thus improves the photocatalytic activity of the samples [41].

By constructing the layered structure film of $Si-Nd_2O_3-TiO_2$, in which the upper TiO_2 crystal film can play the photocatalytic performance. The thickness of the film affects the transmission distance of the film and the propagation distance of the film, which affects the photocatalytic performance. When the film is less than its characteristic thickness (the characteristic thickness of the depletion layer is comparable to the thickness, the depletion layer is the region in which the carriers (electrons and holes) are exhausted by diffusion), the catalytic activity is low; increasing the thickness of the film can increase its catalytic activity, when the temporal catalytic activity is high; when the film thickness is greater than the characteristic thickness, the size of the depletion layer is also related to the doping ratio and the constructed heterojunction area [42]. From the experimental results, the n-*n*-type hetero-junction is formed at the film interface of the composite film to form an internal electric field, and the depletion layer range is 20–25 nm. However, the special certificate thickness of TiO_2 is about 30 nm [43,44]. Therefore, the photocatalytic performance of sample 6 (6-TiO_2 (30 nm) -Nd_2O_3 (70 nm)) is close to that of TiO_2 (100 nm). However, the change in the performance of samples 1 to 3 is due to the dysplasia of the most superficial TiO_2 crystals between the two materials under high temperature annealing. More lattice defects will reduce the photocatalytic activity of TiO_2, because the defects are the trap and recombination center of photoelectron-hole deep capture. Usually, TiO_2 crystals with good lattice defects with less crystallinity are required in order to improve the photocatalytic activity. However, when the thickness of the TiO_2 crystal film on the surface is less than 15 nm, the heterojunction electric field constructed by the both materials is not enough to offset the lattice defects due to the lattice distortion of the both materials after annealing at the high temperature. Therefore, it will lead to reduce its photocatalytic performance [45].
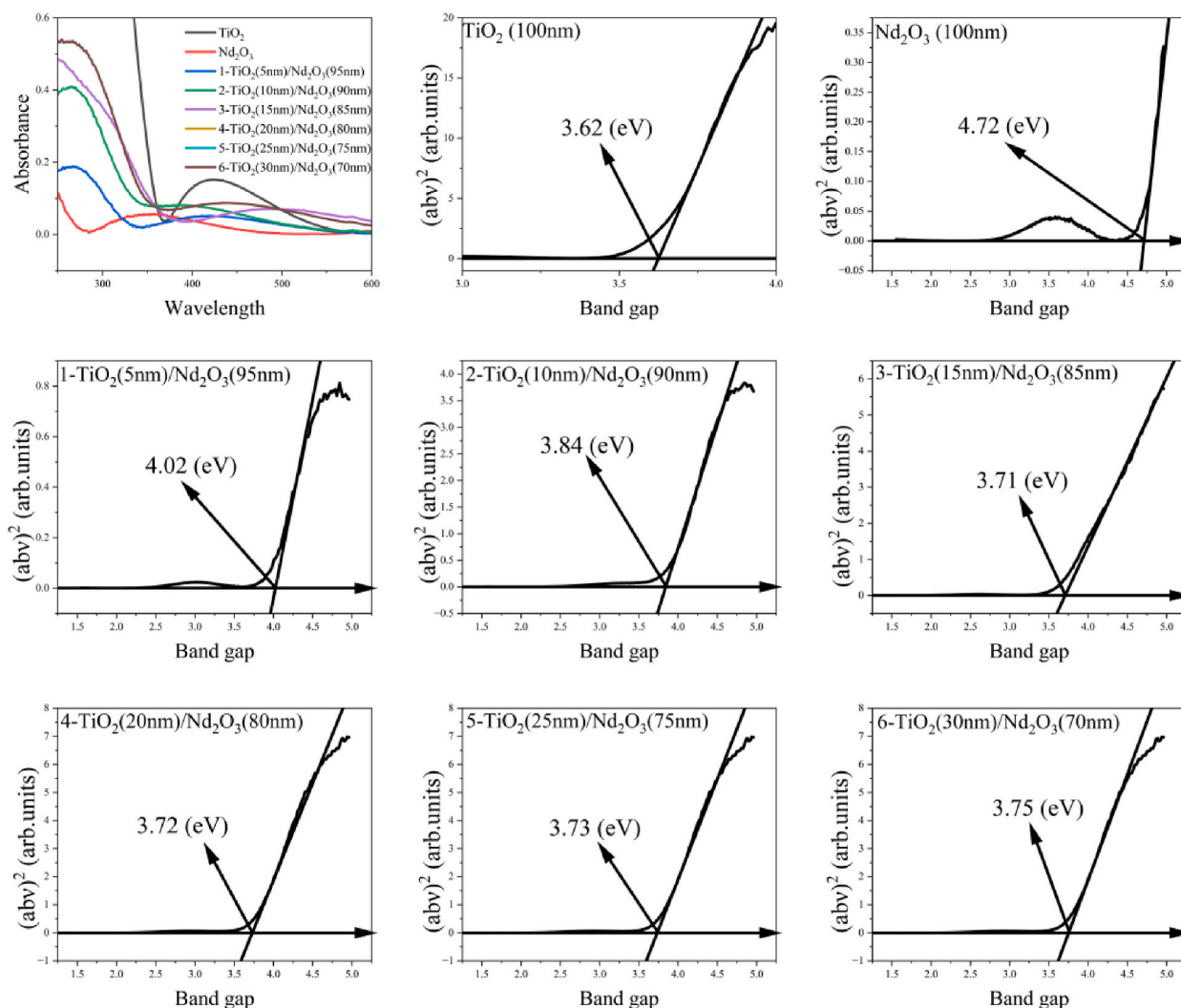
Fig. 16. Transmittance and band gap value estimations.

4. Conclusions

In present work, TiO_2/Nd_2O_3 thin films were fabricated by EB-PVD. The effects of laminated composite structure of TiO_2 and Nd_2O_3 on microstructure, surface morphology, elemental chemical state, and optical properties of the two kinds of thin films were investigated. The main findings are as follows: the fabricated TiO_2 and Nd_2O_3 composite films are dominated by the hexagonal crystal phase of Nd_2O_3, which is concentrated in the XRD patterns. However, a certain amount of TiO_2 crystal phase is mixed into the Nd_2O_3 lattice. This is the reason why there is only a stretching vibration peak about TiO_2 in the Raman pattern, which is mainly dominated by anatase phase. Meanwhile, due to the EB-PVD for the deposition, the surface of all the samples obtained is uniform, dense, and free of large cluster defects. However, due to the valence bonding between the two materials after high-temperature annealing, lattice distortion was induced. This in turn affects the formation of an n-n type homojunction at the interface between the two layers. Thus, an internal electric field is formed inside the composite thin film, which the causes changes in the chemical state of the elements, especially Ti and O elements [46]. This is reflected in the macroscopic changes in transmittance and microscopic changes in the valence band and band gap width. The result improves the separation efficiency of photogenerated electrons and holes, thus increasing the photocatalytic activity. Among the composite structure, the structures of TiO_2 (20 nm)/Nd_2O_3 (80 nm) and TiO_2 (25 nm)/Nd_2O_3 (75 nm) had the highest catalytic activity for the different concentrations of MB solution, and the catalytic activity was increased more than 10 % compared with the pure TiO_2 thin film. TiO_2 and Nd_2O_3 belong to N-type semiconductor, which can be constructed into N–N type heterojunction, in the constructed heterojunction region. When illuminated by light with sufficient excitation energy, inter-band transitions occur on both sides. Meanwhile, due to the different energy levels of the valence and conduction bands, the photogenerated electrons are mainly concentrated in the conduction band of TiO_2, while the holes are concentrated in the valence band of Nd_2O_3. The results show that the photogenerated carriers are separated and have a longer lifetime, increasing the quantum efficiency
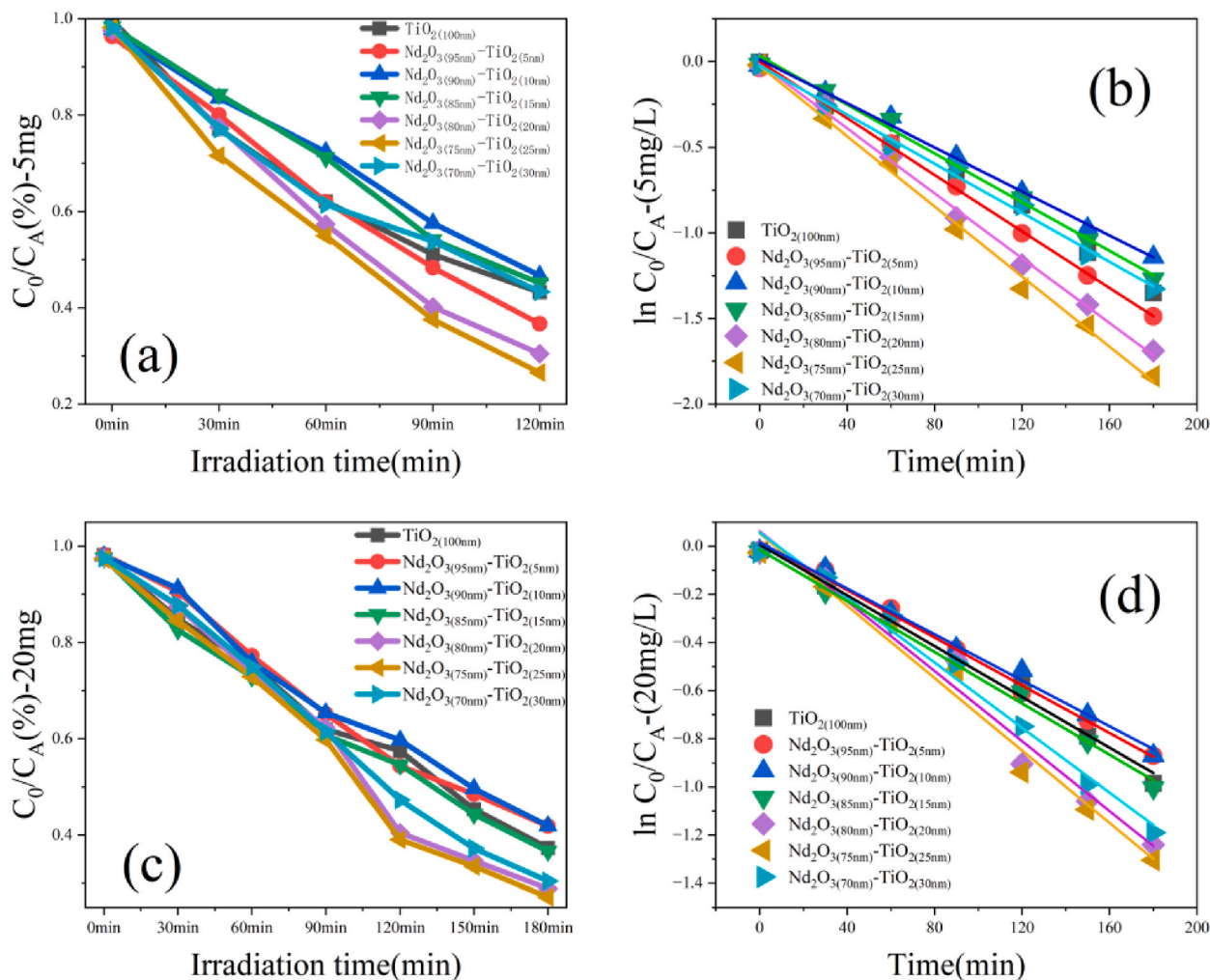
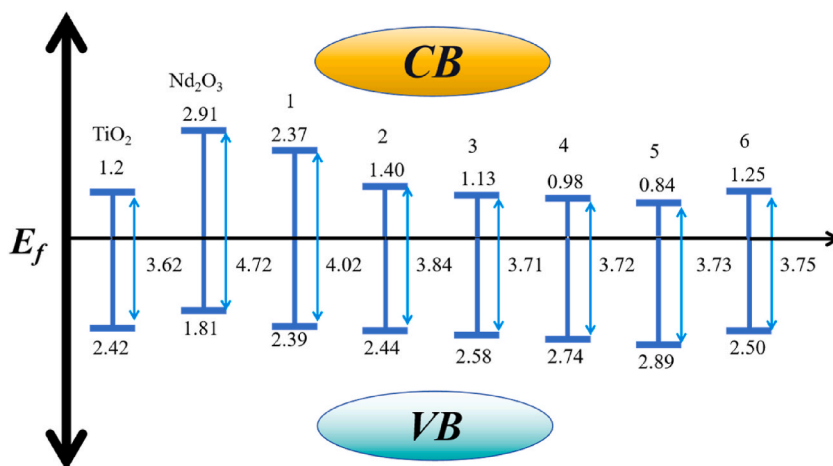**Fig. 17.** Residual percentage of visible light degradation of MB by TiO_2/Nd_2O_3 films.
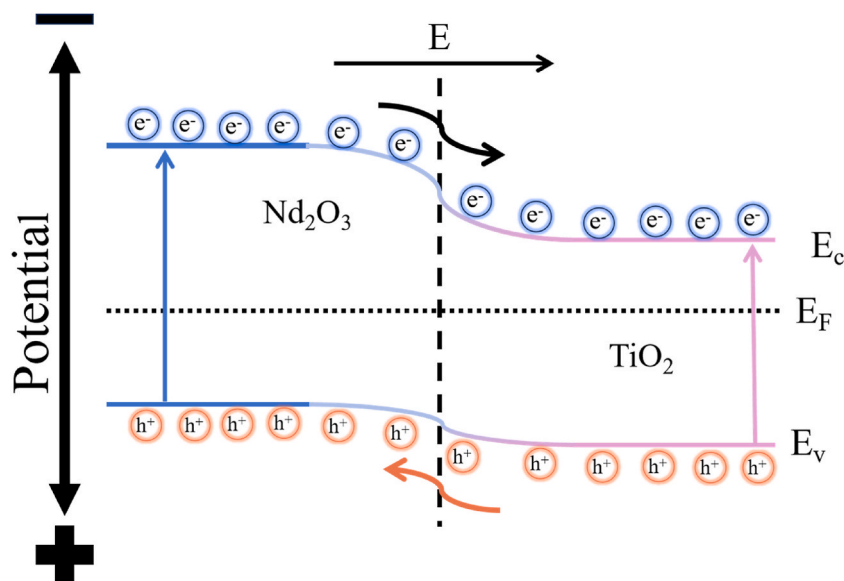

Fig. 18. Energy bands for all the samples.

Fig. 19. Electron flow and inner electric field illustration in the composite TiO$_2$/Nd$_2$O$_3$ thin film.

and reducing the photon-hole composite rate, thus increasing the photocatalytic activity of the sample.

CRediT authorship contribution statement

Guodong Liu: Writing – original draft, Formal analysis, Data curation. **Mamatrishat Mamat:** Writing – review & editing, Software, Project administration, Funding acquisition. **Yiliyasi Baikeli:** Software. **Xiaoshuo Dong:** Supervision, Resources.

Declaration of competing interest

The authors declare the following financial interests/personal relationships which may be considered as potential competing interests:

Yiliyasi Baikeli reports equipment, drugs, or supplies was provided by Dezhou University. If there are other authors, they declare that they have no known competing financial interests or personal relationships that could have appeared to influence the work reported in this paper.

Acknowledgments

References

[1] E. Bet-moushoul, Y. Mansourpanah, K. Farhadi, M. Tabatabaei, TiO$_2$ nanocomposite based polymeric membranes: a review on performance improvement for various applications in chemical engineering processes, Chem. Eng. J. 283 (2016) 29–46.
[2] W. Zhou, H. Fu, Defect-mediated electron–hole separation in semiconductor photocatalysis, Inorg. Chem. Front. 5 (6) (2018) 1240–1254.
[3] G. Di Liberto, L.A. Cipriano, S. Tosoni, G. Pacchioni, Rational Design of semiconductor heterojunctions for photocatalysis, Chem. Eur J. 27 (53) (2021) 13306–13317.
[4] L.P. Zhang, M. Jaroniec, Toward designing semiconductor-semiconductor heterojunctions for photocatalytic applications, Appl. Surf. Sci. 430 (2018) 2–17.
[5] N. Sun, X. Si, L. He, J. Zhang, Y. Sun, Strategies for enhancing the photocatalytic activity of semiconductors, Int. J. Hydrogen Energy 58 (2024) 1249–1265.
[6] T. Su, Z. Qin, H. Ji, Z. Wu, An overview of photocatalysis facilitated by 2D heterojunctions, Nanotechnology 30 (50) (2019).
[7] T. Ahmed, T. Farooq, K. Ahmed, M.A. Ur Rehman, M. Yasir, S. Butt, M.A. Basit, Ensuing the formation of photocatalytic TiO2/Fe2O3 nanocomposite from heat treatment of electrophoretically deposited TiO2 films on stainless steel, Colloids Surf. A Physicochem. Eng. Asp. 691 (2024).
[8] F. Javed, S. Javed, M. Mujahid, F.u. Inam, A.S. Bhatti, Modified optical characteristics of TiO$_2$/Au/TiO$_2$ thin composite films, Ceram. Int. 45 (17) (2019) 22336–22343.
[9] L. Kadri, A. Abderrahmane, G. Bulai, A. Carlescu, C. Doroftei, I. Motrescu, S. Gurlui, L. Leontie, M. Adnane, Optical and structural analysis of TiO$_2$–SiO$_2$ nanocomposite thin films fabricated via pulsed laser deposition technique, Nanomaterials 13 (10) (2023).
[10] X. Li, X. Han, D. Zhu, Y. Chen, L. Li, Z. Ma, Y. Gu, F. Ren, J. Huang, Improvement of photoelectric properties of TiO$_2$/Bi$_2$S$_3$ composite film by annealing treatment, Opt. Mater. 91 (2019) 101–107.
[11] G.-X. Ren, B. Yu, Y.-M. Liu, H.-X. Wang, W.-G. Zhang, W. Liang, High photocatalytic activity of Cu2O/TiO2/Pt composite films prepared by magnetron sputtering, Rare Met. 36 (10) (2016) 821–827.
[12] N. Triamnak, S. Suttiruengwong, N. Vittayakorn, S. Girdthep, R. Khankrua, The properties investigations of PLA/TiO$_2$ and PLA/doped-TiO$_2$ composites films, Polymer-Plastics Technology and Materials 62 (12) (2023) 1576–1586.

[13] S.-Y. Wang, B.-B. Zhu, D.-Z. Li, X.-Z. Fu, L. Shi, Preparation and characterization of TiO$_2$/SPI composite film, Mater. Lett. 83 (2012) 42–45.

[14] Z. Wang, L. Ai, Q. Wu, Preparation and photochromism performance of P$_2$W$_{16}$Mo$_2$/PVA/TiO$_2$composite films, J. Coord. Chem. 73 (17–19) (2020) 2402–2409.

[15] J. Yang, Y. Hu, C. Jin, L. Zhuge, X. Wu, Preparation of TiO$_2$/single layer graphene composite films via a novel interface-facilitated route, Appl. Surf. Sci. 503 (2020).

[16] X. Yuan, W. Xu, F. Huang, Q. Wang, Q. Wei, D. Chen, Structural colors of fabric from Ag/TiO$_2$ composite films prepared by magnetron sputtering deposition, Int. J. Cloth. Sci. Technol. 29 (3) (2017) 427–435.

[17] S.H. Jeon, K. Nam, H.J. Yoon, Y.-I. Kim, D.W. Cho, Y. Sohn, Hydrothermal synthesis of Nd$_2$O$_3$ nanorods, Ceram. Int. 43 (1) (2017) 1193–1199.

[18] G. Sala, M.B. Stone, B.K. Rai, A.F. May, C.R. Dela Cruz, H. Suriya Arachchige, G. Ehlers, V.R. Fanelli, V.O. Garlea, M.D. Lumsden, D. Mandrus, A.D. Christianson, Physical properties of the trigonal binary compoundNd2O3, Phys. Rev. Mater. 2 (11) (2018).

[19] C.H. Kao, H. Chen, Y.-C. Liao, J.Z. Deng, Y.C. Chu, Y.T. Chen, H.W. Chang, Comparison of high-κ Nd$_2$O$_3$ and NdTiO$_3$ dielectrics deposited on polycrystalline silicon substrates, Thin Solid Films 570 (2014) 412–416.

[20] A.A.A. Awshah, U.S.a. Aliyu, H.M. Kamari, I.G. Geidam, R. El-Mallawany, A.M. Hamza, M.N.A. Azis, S.H. Alazoumi, Polarizability and optical properties of TeO$_2$–ZnO glass system doped with Nd$_2$O$_3$, J. Mater. Sci. Mater. Electron. 33 (17) (2022) 13493–13505.

[21] N.A. Narewadikar, R.S. Pedanekar, V.G. Parale, H.H. Park, K.Y. Rajpure, Spray deposited yttrium incorporated TiO$_2$ photoelectrode for efficient photoelectrocatalytic degradation of organic pollutants, J. Rare Earths 41 (12) (2023) 1929–1937.

[22] S. Yildirim, M. Yurddaskal, T. Dikici, I. Aritman, K. Ertekin, E. Celik, Structural and luminescence properties of undoped, Nd^{3+} and Er^{3+} doped TiO$_2$ nanoparticles synthesized by flame spray pyrolysis method, Ceram. Int. 42 (9) (2016) 10579–10586.

[23] J. Cui, G.A. Hope, Raman and fluorescence spectroscopy of CeO$_2$, Er$_2$O$_3$, Nd$_2$O$_3$, Tm$_2$O$_3$, Yb$_2$O$_3$, La$_2$O$_3$, and Tb$_4$O$_7$, Journal of Spectroscopy 2015 (2015) 1–8.

[24] S. Jiang, J. Liu, L. Bai, X. Li, Y. Li, S. He, S. Yan, D. Liang, Anomalous compression behaviour in Nd$_2$O$_3$ studied by x-ray diffraction and Raman spectroscopy, AIP Adv. 8 (2) (2018).

[25] Y. Li, Z. Chen, J. Liu, R. Liu, C. Zhang, H. Li, Novel high entropy oxide as anode for high performance lithium-ion capacitors, Ceram. Int. 49 (23) (2023) 38439–38447.

[26] V. Kumar, W.-F. Chen, X. Zhang, Y. Jiang, P. Koshy, C.C. Sorrell, Properties and performance of photocatalytic CeO$_2$, TiO$_2$, and CeO$_2$–TiO$_2$ layered thin films, Ceram. Int. 45 (17) (2019) 22085–22094.

[27] M. Shao, Y. Huang, J. Liu, X. Jia, K. An, L. Chen, J. Wei, C. Li, Effect of deposition temperature on structure and properties of Nd2O3 thin films prepared by magnetron sputtering, Vacuum 169 (2019).

[28] J.P. Baltrus, M.J. Keller, Rare earth oxides Eu$_2$O$_3$ and Nd$_2$O$_3$ analyzed by XPS, Surf. Sci. Spectra 26 (1) (2019).

[29] Y. Qiao, S. Nie, W. Li, E. Liu, X. Wang, Cobalt diffusion during the initial stage of CVD diamond growth on cemented carbide – a molecular dynamics and experimental study, Appl. Surf. Sci. 633 (2023).

[30] C.R. Michel, A.H. Martínez-Preciado, N.L.L. Contreras, Gas sensing properties of Nd$_2$O$_3$ nanostructured microspheres, Sensor. Actuator. B Chem. 184 (2013) 8–14.

[31] C. Loka, K.-S. Lee, Preparation of TiO$_2$/Ag/TiO$_2$(TAT) multilayer films with optical and electrical properties enhanced by using Cr-added Ag film, Appl. Surf. Sci. 415 (2017) 35–42.

[32] F. Sessa, M. Rahm, Electronegativity equilibration, J. Phys. Chem. 126 (32) (2022) 5472–5482.

[33] B.A. Taleatu, E.A.A. Arbab, G.T. Mola, Synthesis and some surface studies of laminated ZnO/TiO$_2$ transparent bilayer by two-step growth, Mater. Sci. Semicond. Process. 44 (2016) 85–90.

[34] M. Zeljko, S.L. Blagojević, V.O. Bulatović, The role of titanium dioxide surface modification on UV protective properties of eco-friendly PA coating, Prog. Org. Coating 174 (2023).

[35] G. Kilic, Role of Nd3+ ions in TeO$_2$–V$_2$O$_5$–(B$_2$O$_3$/Nd$_2$O$_3$) glasses: structural, optical, and thermal characterization, J. Mater. Sci. Mater. Electron. 31 (15) (2020) 12892–12902.

[36] K. Alshammari, T. Alashgai, A.H. Alshammari, M.M. Abdelhamied, S. Alotibi, A. Atta, Effects of Nd$_2$O$_3$ nanoparticles on the structural characteristics and dielectric properties of PVA polymeric films, Polymers 15 (20) (2023).

[37] S. Zinatloo-Ajabshir, M. Mortazavi-Derazkola, M. Salavati-Niasari, Nd$_2$O$_3$ nanostructures: simple synthesis, characterization and its photocatalytic degradation of methylene blue, J. Mol. Liq. 234 (2017) 430–436.

[38] M.I. Mohammed, I.S. Yahia, D. Elfiky, N. Hesham, A.T. Mosleh, M.S.A. Hussien, Structural, bandgap analysis, electrical properties, and photocatalytic applications of PMMA/Nd$_2$O$_3$ composite membranes: towards multifunctional materials for optoelectronic and environmental applications, J. Inorg. Organomet. Polym. Mater. 34 (2023) 848–863.

[39] Y. Guo, P. Wang, J. Qian, J. Hou, Y. Ao, C. Wang, Construction of a composite photocatalyst with significantly enhanced photocatalytic performance through combination of homo-junction with hetero-junction, Catal. Sci. Technol. 8 (2) (2018) 486–498.

[40] H. Cai, B. Wang, L. Xiong, J. Bi, L. Yuan, G. Yang, S. Yang, Orienting the charge transfer path of type-II heterojunction for photocatalytic hydrogen evolution, Appl. Catal. B Environ. 256 (2019).

[41] X. Meng, S. Wang, C. Zhang, C. Dong, R. Li, B. Li, Q. Wang, Y. Ding, Boosting hydrogen evolution performance of a CdS-based photocatalyst: in situ transition from type I to type II heterojunction during photocatalysis, ACS Catal. 12 (16) (2022) 10115–10126.

[42] A.G. Shende, T. Bhoyar, D. Vidyasagar, J. Singh, P.T. Kosankar, S.S. Umare, Exciton dissociation on double Z-scheme heterojunction for photocatalytic application, ChemistrySelect 6 (26) (2021) 6707–6713.

[43] W. Zhao, S. Liu, Y. Liu, S. Yang, B. Liu, X. Hong, J. Shen, C. Sun, Integration of ohmic junction and step-scheme heterojunction for enhanced photocatalysis, J. Colloid Interface Sci. 654 (2024) 134–149.

[44] B. Zhu, J. Sun, J. Zhao, L. Zhang, J. Yu, Construction of 2D S-scheme heterojunction photocatalyst, Adv. Mater. 36 (8) (2023).

[45] J. Low, J. Yu, M. Jaroniec, S. Wageh, A.A. Al-Ghamdi, Heterojunction photocatalysts, Adv. Mater. 29 (20) (2017).

[46] M. Mokhtar, A. Shawky, Enhanced visible-light-driven H$_2$ evolution over sol-gel prepared Nd2O3 supported with PtO nanoparticles, Ceram. Int. 48 (24) (2022) 36670–36677.